Journal Pre-proofs

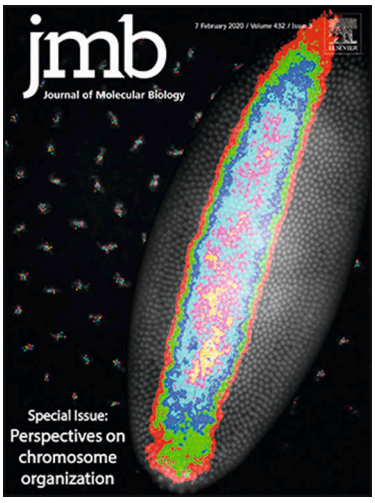

Research Article

Insights into the structural basis of amyloid resistance provided by cryo-EM structures of AApoAII amyloid fibrils

Giada Andreotti, Julian Baur, Marijana Ugrina, Peter Benedikt Pfeiffer, Max Hartmann, Sebastian Wiese, Hiroki Miyahara, Keiichi Higuchi, Nadine Schwierz, Matthias Schmidt, Marcus Fändrich

PII: S0022-2836(24)00007-X
DOI: https://doi.org/10.1016/j.jmb.2024.168441
Reference: YJMBI 168441

To appear in: *Journal of Molecular Biology*

Received Date: 6 October 2023
Revised Date: 20 December 2023
Accepted Date: 4 January 2024

Please cite this article as: G. Andreotti, J. Baur, M. Ugrina, P. Benedikt Pfeiffer, M. Hartmann, S. Wiese, H. Miyahara, K. Higuchi, N. Schwierz, M. Schmidt, M. Fändrich, Insights into the structural basis of amyloid resistance provided by cryo-EM structures of AApoAII amyloid fibrils, *Journal of Molecular Biology* (2024), doi: https://doi.org/10.1016/j.jmb.2024.168441

Insights into the structural basis of amyloid resistance provided by cryo-EM structures of AApoAII amyloid fibrils

Giada Andreotti[1]*, Julian Baur[1], Marijana Ugrina[2], Peter Benedikt Pfeiffer[1], Max Hartmann[1], Sebastian Wiese[3], Hiroki Miyahara[4], Keiichi Higuchi[4,5], Nadine Schwierz[2], Matthias Schmidt[1], Marcus Fändrich[1]

Affiliations

[1] Institute of Protein Biochemistry, Ulm University, 89081 Ulm, Germany.

[2] Institute of Physics, University of Augsburg, 86159 Augsburg, Germany.

[3] Core Unit Mass Spectrometry and Proteomics, Ulm University, 89081 Ulm, Germany.

[4] Institute for Biomedical Science, Shinshu University, Matsumoto 390-8621, Japan.

[5] Faculty of Human Health Sciences, Meio University, Nago 905-8585, Japan.

Correspondence

*Correspondence to: giada.andreotti@uni-ulm.de

Abstract

Amyloid resistance is the inability or the reduced susceptibility of an organism to develop amyloidosis. In this study we have analysed the molecular basis of the resistance to systemic AApoAII amyloidosis, which arises from the formation of amyloid fibrils from apolipoprotein A-II (ApoA-II). The disease affects humans and animals, including SAMR1C mice that express the C allele of ApoA-II protein, whereas other mouse strains are resistant to development of amyloidosis due to the expression of other ApoA-II alleles, such as ApoA-IIF. Using cryo-electron microscopy, molecular dynamics simulations and other methods, we have determined the structures of pathogenic AApoAII amyloid fibrils from SAMR1C mice and analysed the structural effects of ApoA-IIF-specific mutational changes. Our data show that these changes render ApoA-IIF incompatible with the specific fibril morphologies, with which ApoA-II protein can become pathogenic in vivo.

Keywords

Aggregation, protein misfolding, amyloidosis, apolipoprotein, amyloid resistance

Abbreviations

ApoA-II, apolipoprotein A-II; serum amyloid A (SAA); HDL, high density lipoprotein; ApoA-IIC, ApoA-II type C; ApoA-IIF, ApoA-II type F; cryo-EM, cryo-electron microscopy; MS, mass spectrometry; PTM, post translational modification; TEM, transmission electron microscopy; FSC, Fourier shell correlation; MD, molecular dynamics; RMSD, root mean square deviation.

Introduction

Amyloid resistance refers to the inability or the reduced susceptibility of an organism to develop amyloidosis. Examples of amyloid resistance have been provided for several amyloid diseases, including Alzheimer's[1,2], the prion disease kuru[3,4] and murine systemic AA amyloidosis[5]. Although the molecular basis of amyloid resistance is not well-understood, it is typically found to be associated with changes in the gene of the amyloid fibril precursor protein. For example, the Ala673Thr mutation of the amyloid-β precursor protein confers protection against Alzheimer's disease[1,2]. The Gly127Val mutation of the prion protein renders members of the Fore tribe in Papua-New Guinea resistant to kuru[3]. Heterozygosity at position 129 (Met or Val) of the prion protein is protective against Creutzfeldt-Jakob[6] and Gerstmann-Sträussler-Scheinker diseases[7]. In murine systemic AA amyloidosis, it was found that the amyloid resistance arises from the expression of a variant serum amyloid A (SAA) protein and in particular from SAA2.2 protein[5,8].

In the present study we investigate the phenomenon of amyloid resistance in case of systemic AApoAII amyloidosis. This protein misfolding disease is caused by the deposition of amyloid fibrils derived from apolipoprotein A-II (ApoA-II) protein. ApoA-II is a blood-borne apolipoprotein that is mostly bound to high density lipoprotein (HDL) particles and mediates the reverse cholesterol transport from the peripheral organs to the liver[9]. The associated amyloid disease can affect both humans and animals[10,11]. It constitutes an example of amyloid resistance – specifically in mice, as both amyloid-resistant and amyloid-susceptible mouse strains have been described. For example, the strain SPRET/Ei of *Mus spretus* resists the development of AApoAII amyloidosis even if these mice receive intravenous injections of AApoAII amyloid fibrils[12]. SPRET/Ei mice differ in this property to SAMR1C mice, which rapidly develop AApoAII amyloidosis under comparable conditions[13].

The amyloid resistance of SPRET/Ei mice is thought to arise from the expression of a specific allelic variant of ApoA-II protein. While SAMR1C mice express the C allele of ApoA-II protein (ApoA-IIC)[14], SPRET/Ei mice express ApoA-IIF[12,14]. The two protein variants differ at only four positions of the amino acid sequence. Two changes (Ser9Asn and Arg54Lys) are chemically conservative, while the other two (Gln16His and Asn62Lys) replace a polar residue with an ionizable one. All mutations are reported here in the direction from C to F. The Asn62Lys mutation has been suggested, based on biochemical evidence, to be particularly crucial for this effect, as an ApoA-IIF-derived peptide fragment that carries the Asn62Lys mutation inhibited the formation of amyloid fibrils in ApoA-IIC expressing mice[12]. Yet, the specific role of this mutation in systemic AApoAII amyloidosis remains elusive as both involved residues (Asn and Lys) occur abundantly in the ordered core of other amyloid fibril structures.

To investigate the structural basis of amyloid resistance in AApoAII amyloidosis, we have determined the structures of AApoAII fibrils that we isolated from diseased mice. Using cryo-electron microscopy (cryo-EM), we find that the sample contains two main fibril morphologies, which consist of a common fibril protein fold. Comparison of the experimentally determined fibril structures, which are based on ApoA-IIC protein, with hypothetical ApoA-IIF-based structural homologues provided strong evidence that the sequence of ApoA-IIF is incompatible with the specific fibril morphologies underlying the development of disease.

Results

Murine AApoAII amyloid fibrils are proteinase K stable

AApoAII amyloid fibrils were isolated from the livers of four SAMR1C mice, which express ApoA-IIC protein. The mice were sacrificed at an age of 9 to 17 months when they suffered from severe systemic amyloidosis. Denaturing gel electrophoresis reveals one dominant fibril protein species with an apparent molecular weight of ~6 kDa (Supplementary Fig. 1a), which is consistent with previously reported gel electrophoretic measurements[15]. The fibrils are resistant to proteinase K digestion (Supplementary Fig. 1) and roughly one third of the fibril protein survives proteolysis for 1 h (Supplementary Fig. 1b). Consistent results in this regard were obtained with the fibrils from four animals (Supplementary Fig. 1). We conclude that ex vivo AApoAII amyloid fibrils are more stable to proteolysis than most in vitro formed amyloid fibrils which become fully degraded under comparable experimental conditions[16,17].

Murine AApoAII amyloid fibrils are post-translationally modified

Using mass spectrometry (MS) we could identify several primary structural variants of the fibril protein. The most abundant fibril protein, as judged by the peak intensity, corresponds to full-length ApoA-II (Supplementary Fig. 2, Supplementary Tables 1-4) but we found, in addition, several shorter fibril proteins that constitute fragments of ApoA-IIC protein. These fragments lack the first one or two residues or they are C-terminally truncated between residues 54 and 77 (Fig. 1). All fibril proteins starting with residue 1 contain a N-terminal pyroglutamate (Supplementary Tables 1-4). In addition, we found a variable oxidation of the three methionine residues of the protein and the formation of sulfonates or sulfones (Supplementary Tables 1-4). Up to three extra oxygen atoms (+16 Da each) could be discerned in a fibril protein (Supplementary Fig. 3). The fibrils from all four animals analysed here show similar fragment length variations and post-translational modifications (PTMs) (Supplementary Tables 1-4).

Murine AApoAII amyloid fibrils occur in two main fibril morphologies

Transmission electron microscopy (TEM) shows that AApoAII amyloid fibrils occur in two main fibril morphologies, termed here Morphologies I and II (Supplementary Fig. 4). The two fibril structures are visible in negatively stained (Supplementary Fig. 4) and cryo-frozen samples (Fig. 2, Supplementary Fig. 5) and were found in the isolated fibril samples from all four animals (Supplementary Fig. 4). TEM combined with platinum side shadowing demonstrates the left-hand fibril twist of the fibrils (Supplementary Fig. 6). Based on cryo-EM, Morphology I possesses a width of 9.9 ± 0.7 nm and a cross-over distance of 110.6 ± 7 nm (n = 20), while Morphology II has a width of 20.1 ± 0.8 nm and a cross-over distance of 146.3 ± 9.4 nm (n = 20). Approximately 75 % of the fibrils visible by cryo-EM correspond to Morphology I, while ~23 % of the fibrils correspond to Morphology II (Fig. 2). In addition, we could identify a third filament type (Morphology III), which exhibits a width of 11.1 ± 1.2 nm and a cross-over distance of 65.7 ± 5.7 nm (Fig. 2). However, this fibril type was too rare to be further analysed.

Cryo-EM structures of AApoAII fibril morphologies I and II

Reconstruction of the three-dimensional (3D) maps of fibril Morphologies I and II achieved resolutions of 2.4 Å and 2.6 Å, based on the 0.143 Fourier shell correlation (FSC) criterion (Supplementary Fig. 8, Supplementary Table 6). The 3D maps revealed that both fibrils are polar and pseudo 2_1 screw symmetrical (Supplementary Fig. 7a). The 3D maps implement the left-hand twist which we established by platinum side shadowing (Supplementary Fig. 6). Analysis of the fibril cross-sections shows that both fibrils are constructed from structurally similar fibril protein stacks. There are two stacks in Morphology I and four in Morphology II. The latter morphology contains two topologically different protein stacks: type A stacks close to the z-axis, and type B protein stacks at an outer radial positions (Fig. 3b). Interpretation of the 3D maps with molecular models (Fig. 3a, Supplementary Table 7) shows that the ordered structure extends, in all protein stacks, from Gly4 to Glu71 (Fig. 3). That is, the first three (Gln1-Asp3) and the last seven residues (Glu72-Ala78) of ApoA-IIC are conformationally disordered or proteolytically truncated in the fibril. Hence, they are not seen in our 3D maps.

Fibril protein fold and internal cavities of the fibril structure

The structure of the fibril protein is almost identical irrespective of the fibril morphology or topological position within the fibril structure (Fig. 4). The proteins belong to the all-beta class of protein folds and show small variations with respect to the exact lengths of the eleven β-strands (β1-β11) (Fig. 4). All strands participate in the formation of cross-β sheets with uniformly parallel intra-sheet strand-strand interactions (Fig. 4a). The fibrils enclose two types of cavities: one cavity type occurs at the centre of each fibril protein stack while the second one occurs only in Morphology II and at the interface between two type A fibril protein stacks (Supplementary Fig. 10). All cavities seem to be water-filled (Supplementary Fig. 11) as they are lined with polar or charged amino acid residues. In addition, we found weak density features at conserved sites within these cavities that could arise from bound water molecules (Supplementary Fig. 11). There was no evidence for the involvement of other molecular inclusions, such as hydrophobic molecules, which were occasionally reported for ex vivo amyloid fibril structures[18–20].

The reconstructed 3D maps are ambiguous at three residues (Met7, Leu10 and Leu25) and allow the placement of different chain rotamers (Supplementary Fig. 12). The three residues are solvent exposed and point either towards one of the cavities or to the bulk solvent. It remains to be established whether the different side chain rotamers occur in different molecular layers of the same fibril or whether they represent different morphological sub-states of the fibril that are associated with different side-chain conformers and became averaged during reconstruction. In case of residue Met7, however, it is alternatively possible that the ambiguous density arises from the oxidation of this residue.

Non-covalent interactions within the fibril structure

The fibril protein stacks are stabilised by clusters of hydrophobic residues, such as the clusters formed by Val26, Ala29 and Ile34 or Leu49, Val61 and Phe63 (Supplementary Fig. 7, Fig. 4). In addition, we find juxtaposed residues of complementary charge at buried positions, suggesting the involvement of electrostatic interactions (Supplementary Fig. 13). Some of these interactions run across different molecular layers of the fibril, which may sterically interlock the filaments. Indeed, the fibril protein molecules shows an axial elevation of 8.7 Å in Morphology I and of 12.1 Å in Morphology II which was measured between the highest and the lowest C_α atom. This elevation interdigitates the different layers of the fibril. Additional stabilising interactions may come from the staggering of adjacent protein stacks in the pseudo 2_1-screw symmetrical fibrils (Supplementary Fig. 9a). There are two contact modes between adjacent protein stacks. One contact mode is formed by a tight and self-complementary packing of residues Gln5 to Gln15 (Supplementary Fig. 9b). This mode occurs between the two protein stacks of Morphology I or between type A and type B fibril protein stacks of Morphology II (Supplementary Fig. 9b). The second type of contact mode occurs only in Morphology II and between two type A fibril protein stacks (Supplementary Fig. 9b). This contact mode involves interactions between residues Lys30 in one stack and Glu43 in the other protein stack (Supplementary Fig. 9b).

Structural basis of amyloid resistance in mice

The resistance and susceptibility of different mouse strains to development of AApoAII amyloidosis is thought to arise from the expressed allele of ApoA-II protein. ApoA-IIC is expressed in mouse strain, which we used here to extract AApoAII amyloid fibrils, and is known to be highly amyloidogenic in vivo[12]. ApoA-IIF, by contrast, renders animals amyloid resistant[12]. To investigate the possible effect of the four residues that are different in ApoA-IIF and ApoA-IIC (Fig. 5), we constructed a homology model of the experimentally determined fibril, which is based on the sequence of ApoA-IIF (Fig. 5). The model shows that all four mutational changes of ApoA-IIF affect internal residues. Arg54Lys and Asn62Lys are buried within the fibril protein stack, while Ser9Asn and Gln16His are buried at the interface between the two juxtaposed protein stacks.

To clarify the role of these mutations, we performed molecular dynamics (MD) simulations with the experimentally determined structure and the ApoA-IIF-based homology model. The simulations show that the experimentally determined structure is stable over time (200 ns) and does not deviate much from the starting structure (Fig. 5c, Supplementary Fig. 14). By contrast, the ApoA-IIF-based homology model shows much larger deviations from the starting structure over the course of the simulation (Fig. 5c). Hence, the mutational changes in ApoA-IIF destabilise the fibril and cause a progressive loosening of its compact conformation.

To investigate which of the four mutational changes is most crucial for this effect, we generated homology models, in which each of the four mutations of ApoA-IIF was inserted individually into the ApoA-IIC-derived fibril Morphology I (Supplementary Fig. 14). Based on these simulations, we find the strongest destabilising effect in case of the model containing the mutational change Asn62Lys (Supplementary Fig. 14). Additionally, we analysed the contribution of the intra- and intermolecular interactions between the atoms of the fibril

proteins to the total energy (see Methods section for details). Based on this analysis we find that the interaction energy of AApoA-IIC fibrils is -20.3 ± 0.5 MJ/mol, while the ApoA-IIC Asn62Lys mutant has an interaction energy of -16.8 ± 0.06 MJ/mol, which further confirms the view that the mutation is destabilizing to the fibril structure. The importance of residue Asn62 for the specific morphology of pathogenic AApoAII amyloid fibrils, which we revealed here by cryo-EM and MD simulations, corroborate the previous biochemical findings that the amyloid resistance of ApoA-IIF expressing mice arises primarily from the change at position 62[12]. Therefore, our data explain the phenomenon of amyloid resistance with the insertion of a positively charged residues at structurally important site of the protein fold. In other words, ApoA-IIF is incompatible with the specific structure of the pathologically relevant fibril structure.

Discussion

Previous research established that mice expressing the F allele of ApoA-II protein are amyloid resistant, while mice that express the C allele are able to develop the disease[12,14]. The resistance could not be attributed to any other physiological parameter of the animals than the allele of ApoA-II protein[12]. Hence, it arises from four mutagenic changes in ApoA-IIF compared to ApoA-IIC. In the present study, we have obtained cryo-EM structures of the two major ex vivo AApoAII amyloid fibril morphologies (Fig. 2) and we investigated the structural properties of AApoAII fibrils with MD simulations (Fig. 5) and other methods. We identified the mutation Asn62Lys as particularly crucial for the amyloid resistance of ApoA-IIF expressing animals as it was found to be specifically incompatible with the structural morphology of the pathogenically relevant fibril morphology (Supplementary Fig. 14). These data are consistent with and provide a structural explanation for previous biochemical evidence indicating the importance of the Asn62Lys mutation[12].

Our current data - and in particular our conclusion that the amyloid resistance in systemic AApoAII amyloidosis arises from the incompatibility of the mutant form of the protein with the pathogenic fibril structure - are consistent with previous data on the molecular origins of the amyloid resistance of mice with systemic AA amyloidosis[5]. This protein misfolding disease arises from the aggregation of serum amyloid A (SAA) protein[21]. SAA is part of a larger protein family, and mice naturally express several SAA family members and allelic variants. Mouse strains that express SAA1.1 are able to develop the disease, while mice that express SAA2.2 and SAA1.5 are amyloid resistant[5,8]. Strong genetic evidence exists that the two proteins are causative for this effect[8]. SAA1.5 differs at three position from SAA1.1 protein[8], SAA2.2 differs at six position, including the three changes from SAA1.5. Based on the cryo-EM structure of the pathogenic fibril, we identified the mutation Gly7His as particularly important, as it placed a charged residue into the hydrophobic core of the pathogenic fibril morphology[8]. Therefore, amyloid resistance in systemic AA amyloidosis also arises from the incompatibility of the variant fibril protein with the pathogenically relevant fibril morphologies - similar to what we find here for AApoAII amyloidosis.

Our conclusions have potential ramifications for several other amyloid diseases for which there is evidence for amyloid resistance. Examples include Alzheimer's disease and several prion diseases[3,4,6,7]. While the exact mechanisms of amyloid or prion resistance are not established in all cases, also an altered cellular processing of the fibril precursor protein has been discussed[1], it is a common observation that amyloid resistance involves mutational changes in the amyloid precursor proteins. These data imply that the misfolding of these proteins is important for triggering the respective disease, and that the down-regulation of this protein or its deletion is a possible strategy to prevent the disease, as was shown early by the resistance of mice to prion diseases upon transgenic knockout of the prion protein[4,22].

The specific importance of the fibril morphology for the phenomenon of amyloid resistance implied here represents further evidence that the fibril morphology is crucial for pathology and that only some, but not all, amyloid fibril morphologies are able to give rise to disease. This concept arose previously from observations that the structures of disease-associated amyloid fibrils are different from in vitro formed fibrils[16,23,24]. The structural difference correlate with a different proteolytic resistance of ex vivo and in vitro fibrils[16,17], that is, ex vivo fibrils are more resistant to proteolysis, suggesting that pathogenic amyloid fibrils were selected inside the body by their higher proteolytic stability (proteolytic selection hypothesis)[16,17]. And indeed, we find AApoAII amyloid fibrils to be relatively resistant to proteolysis (Supplementary Fig. 1), similar to the fibrils purified from other forms of systemic AA amyloidosis[19,20,36]. Our data underscore further the importance of working with ex vivo amyloid fibril when drawing conclusions about the structural and molecular principles of misfolding as they are relevant in the course of disease.

Methods

Animal experiments

SAMR1C mice are a congenic strain with the amyloidogenic *Apoa2*^{c} allele on the genetic background of the SAMR1 strain[26]. Mice were raised at the Division of Animal Research, Research Center for Support of Advanced Sciences, Shinshu University, under specific pathogen-free conditions at 24 ± 2 °C with a controlled light regimen (12-h light/dark cycle). A commercial diet (MF; Oriental Yeast) and tap water were available ad libitum. AApoAII amyloidosis in SAMR1C mice can be induced systemically by injection of a small amount of AApoAII amyloid fibrils[27]. One to two-month-old SAMR1C mice were induced AApoAII amyloidosis by intravenous injection with a single dose of 100 µg of extracted AApoAII fibrils, which were isolated from amyloid-laden livers as we previously described[28]. Mice were sacrificed by cardiac puncture under deep sevoflurane anesthesia. Organs including livers were snap-frozen in liquid nitrogen and stored at -80°C. All experiments were performed with the approval of the Committee for Animal Experiments at Shinshu University (Approval No. 300019).

Fibril extraction from mouse tissue

AApoAIIC amyloid fibrils were extracted from an amyloid-laden liver of 9 to 17-months old SAMR1C mice: 9 months (mouse 1), 12 months (mouse 2 and 3) and 17 months (mouse 4). In brief, 60 mg of frozen liver tissue were thawed and diced with a scalpel until no pieces were visible. The suspension was washed five times with 240 µl tris (hydroxymethyl) aminomethan (Tris) calcium buffer (TCB 20 mM Tris, 138 mM NaCl, 2 mM $CaCl_2$, 0.1 % (w/v) NaN_3, pH 8.0) and spun down by centrifugation at 3,100 ×g for 5 min at 4 °C. In each TCB washing step, the pellet was homogenised with a pellet pestle. The final pellet was resuspended in 240 µl freshly prepared collagenase/protease inhibitor solution (one tablet of cOmplete ethylenediamine-tetraacetic acid (EDTA)-free protease inhibitor (Roche) in 7 ml TCB, containing 5 mg/mL crude collagenase from *Clostridium histolyticum* (Sigma) and incubated overnight at 37 °C at 750 rpm in an IKA MTS 2/4 digital table shaker. The suspension was centrifuged at 4 °C and 3,100 ×g for 30 min. The pellet was resuspended in 240 µl Tris EDTA buffer (20 mM Tris, 140 mM NaCl, 10 mM EDTA, 0.1 % (w/v) NaN_3, pH 8.0) and homogenized with a pellet pestle. The homogenate was centrifuged for 5 min at 3,100 at 4 °C and the supernatant was removed. The resuspension in Tris EDTA buffer and centrifugation of the sample was repeated four more times. The resulting pellet was homogenised by a pellet pestle in 240 µl ice cold water. The homogenate was centrifuged for 5 min at 3,100 ×g at 4 °C and the fibril containing supernatant was stored. This water extraction step was repeated seven more times, resulting in eight fibril-containing supernatant fractions.

Mass spectrometry

An aliquot of the amyloid fibril sample was lyophilized and the amount of fibrils was determined by weighting. The dry fibrils were disaggregated by dissolving them in 6 M guanidine hydrochloride containing 50 mM Tris, pH 8.0, to reach a concentration of approximately 0.5 mg/ml. After incubation of the sample at 4 °C overnight, the sample was stored at -20 °C. An aliquot containing 1 µg of disaggregated fibrils was removed and diluted with 0.1 % (v/v) trifluoracetic acid (TFA) to a total volume of 15 µl and immediately analysed with an Orbitrap Elite system (Thermo Fisher Scientific) online coupled to an U3000 RSLCnano (Thermo Fisher Scientific) employing an Acclaim® PepMapTM analytical column (ID: 75 µm x 500 mm, 2 µm, 100 Å, Thermo Fisher Scientific) in combination with a C18 µ-precolumn (0.3 mm inner diameter x 5 mm; PepMap, Dionex LC Packings, Thermo Fisher Scientific). Samples were preconcentrated and washed with 0.1 % (v/v) TFA for 5 min at a flow rate of 30 µl/min. Subsequent separation was carried out employing a flow rate of 250 nl/min using a binary solvent gradient consisting of solvent A (0.1 % (v/v) fluoracetic acid) and solvent B (86 % (v/v) acetonitrile, 0.1 % (v/v) fluoracetic acid). The main column was initially equilibrated in 5% solvent B. The percentage of B was raised from 5 % to 15 % in 10 min, followed by an increase from 15 % to 40 % solvent B in 20 min. The column was washed with an increase to 95 % solvent B in 5 min and holding at 95 % B for 5 min. Finally, the column was re-equilibrated with 15 % solvent B for 20 min.

The mass spectrometer was equipped with a nanoelectrospray ion source and distal coated SilicaTips (FS360-20-10-D, New Objective). The system was operated using the following

parameters: spray voltage, 1.5 kV; capillary temperature, 250°C; S-Lens RF Level, 68.9 %. XCalibur 2.2 SP1.48 (Thermo Fisher Scientific) was used for data-acquisition. Full scans ranging from m/z 370 to 1,700 were acquired in the Orbitrap at a resolution of 30,000 (at m/z 400) with automatic gain control enabled and set to 10^6 ions and a maximum fill time of 500 ms. The recorded mass spectra were summed using Thermo Xcalibur 3.0.63 (Thermo Fisher Scientific) and deconvoluted using the "Quick deconvolution" feature of MASH Explorer[29], which was used with default settings. To exclude noise and artefacts, we retained only monoisotopic peaks with a confidence score of 90 % or more that arose from original m/z peaks with five or more charges. The resulting spectra are shown in Supplementary Fig. 2 and 3. The deconvoluted peaks were assigned to ApoA-IIF protein fragments using the mMass software, using a tolerance of 0.1 Da and a peak charge of 0. In the assignment, we considered methionine oxidation and pyroglutamylation as possible PTMs.

Cryo-EM

A 2.5 µl aliquot of the isolated fibrils from mouse 4 was applied to a glow-discharged holey carbon coated grid (400 mesh C-flat 1.2/1.3), blotted with filter paper and plunge-frozen in liquid ethane using an Automatic Plunge Freezer EM GP2 (Leica microsystems). Grids were optimised by analysing their quality with a JEM-2100 transmission electron microscope (Jeol) at 200 kV, equipped with TVIPS F416 camera. The 300 kV data set for cryo-EM reconstructions was acquired using a Quantum K2 detector (Gatan), which was operated in counting mode and mounted on a Titan Krios transmission electron microscope (Thermo Fisher Scientific). Data acquisition parameters are listed in Supplementary Table 5. Measurements of fibril width and crossover distance were carried out by using Fiji[30].

Helical reconstruction

Motion correction and dose-weighting was done using MOTIONCOR 2.1[31]. The contrast transfer function was estimated from the motion-corrected images using CTFFIND-4[32]. Helical reconstruction was performed using RELION 3.1.2[33]. Fibrils of each morphology were picked manually. Segments were extracted as listed in the Supplementary Table 6. Reference-free 2-dimensional class averaging with a regularisation value of T=2 was used to select classes showing the helical repeat at ~ 4.7 Å along the fibril z-axis. As initial 3D model a featureless cylinder was used that was created by using relion_helix_toolbox which is implemented in RELION. The generated 2D classes of Morphology I indicated the presence of two identical protein stacks; while the one of Morphology II shows 4 protein stacks related by a pseudo-2_1 screw symmetry. Imposing this symmetry during the reconstruction improved the 3D maps. All the particles were retained after the 2D classification. No particles were excluded at the 3D classification stage and a 3D auto-refinement with a local optimization of helical parameters was performed. Post-processing yielded a map resolution of 2.9 Å for both fibril morphologies. Bayesian polishing helped to further improve the reconstruction: the resulting maps, which were subjected to soft-edged masking and B-factor sharpening, had final resolutions of 2.4 Å and 2.6 Å for Morphology I and Morphology II, respectively. The resolutions of the individual reconstructions were estimated from the FSC at 0.143 between two independently refined half-maps.

Model building

The molecular models of Morphologies I and II were built *de novo* in Coot[34] based on the density maps. The structural refinement was done with using real space refinement in Coot implementing restraints on the torsion angles, Ramachandran angles and β-strands. Atomic clashes, rotamer and Ramachandran outliers and the model geometry were evaluated by the Comprehensive Validation tool in Phenix[35], implementing the program MolProbity[36]. Once a satisfactory fit was achieved for one polypeptide chain, a fibril stack comprising of six fibril protein layers was assembled using the pdbsymm tool implemented in Situs[37] and subjected to an iterative refinement until the fit was reasonable. The structural statistics for model building are listed in Supplementary Table 7. Images of the 3D maps and the models were created with UCSF Chimera[38] and Coot.

MD simulations

We performed all-atom MD simulations of the cryo-EM structure of Morphology I and different homology models based on the four mutations of ApoA-IIF. In the ApoA-IIF-based homology model, we replaced all four residues that are different in ApoA-IIF and ApoA-IIC. In four additional models, one of the four mutations was inserted such that each model had only one of the following mutations: Ser9Asn, Gln16His, Arg54Lys or Asn62Lys. The PDB Manipulator tool of the CHARMM-GUI web-interface was used to introduce the mutations[39]. Each fibril structure was placed in a cubic simulation box with a size of 149.6 Å. The boxes were filled with water and neutralized with 0.15 M NaCl, leading to system sizes of about 437,724 atoms. The force field parameters for the proteins were taken from the Amber99sb-star-ildn force field[40] and the TIP4P-Ew[41] model was used for water. For NaCl, we used the Mamatklulov-Schwierz force field parameters[42].

We calculated the total energy from the MD trajectories. To gain insights into the contribution of the intra- and intermolecular interactions between the atoms of the fibril proteins to the total energy, we used a simulation rerun as implemented in Gromacs. In the rerun, the system was divided into the individual components and the energies of the individual groups were calculated as described previously[43]. Standard deviations were calculated from block averaging using five equal blocks.

The MD simulations were performed using the Gromacs simulation package, version 2020.7[44]. The systems were simulated at constant number of particles *N*, pressure *P* and temperature *T*. Periodic boundary conditions were applied, and the particle-mesh Ewald method was used for the periodic treatment of Coulombic interactions. Bonds to hydrogen atoms were constrained using the LINCS algorithm and a 2 fs time step was used. To equilibrate the systems, we first performed an energy minimization with the steepest descent algorithm. The systems were equilibrated for 1 ns, first in the *NVT* and then in the *NPT* ensemble. For the production run, we performed 200 ns long simulations employing the velocity-rescaling thermostat with a stochastic term and a time constant $\tau_T = 0.1ps$ and isotropic Parrinello-Rahman pressure

coupling with a time constant of $\tau_P = 5ps$. The root mean square deviation (RMSD) was calculated from each of the production runs, with the respective experimental or homology modelled structure as reference.

Statistical analysis

The error bars in the paper represent the standard deviation. The standard deviation of the maps used to show the extra density features in Supplementary Fig. 12 was calculated on a noise region cut out of the unmasked maps.

Data availability

The reconstructed cryo-EM maps are deposited in the Electron Microscopy Data Bank with the accession codes **EMD-17105** and **EMD-17104**. The coordinates of the fitted atomic models are deposited in the Protein Data Bank under the accession code **8OQ5** and **8OQ4**. The datasets used in the current study are available from in EMPIAR with the accession code **EMPIAR-11525**.

Acknowledgements

The positions of G.A. an J.B. were funded partly through a grant from the Deutsche Forschungsgemeinschaft (Research Unit FOR 2969, projects FA 456/27-1 and HA 7138/3). The position of M.S. is funded through DFG grant FA 456/28-1. All cryo-EM data were collected at the European Molecular Biology Laboratory, Heidelberg (Germany), funded by iNEXT (Horizon 2020, European Union). We would like to thank Paul Walther (Central Facility for Electron Microscopy, Ulm University) and Felix Weis (EMBL Heidelberg) for technical support. K.H. is supported by the JSPS Core-to-Core Program A (Advanced Research Networks): an international cutting-edge network for the study of protein aggregation.

Author contributions

G.A., J.B., M.U., P.B.P., M.H., S.W. and H.M. carried out experiments. G.A., J.B., M.U., P.B.P., N.S., M.S., K.H. and M.F. analysed data. H.M. and K.H. contributed materials. M.F. designed research. G.A. and M.F. wrote the paper with contributions from all other authors.

References

1. Jonsson, T. *et al.* A mutation in APP protects against Alzheimer's disease and age-related cognitive decline. *Nature* **488**, 96–99 (2012).

2. Di Fede, G. *et al.* A recessive mutation in the APP gene with dominant-negative effect on amyloidogenesis. *Science* **323**, 1473–1477 (2009).

3. Asante, E. A. *et al.* A naturally occurring variant of the human prion protein completely prevents prion disease. *Nature* **522**, 478–481 (2015).

4. Steele, A. D., Lindquist, S. & Aguzzi, A. The Prion Protein Knockout Mouse. *Prion* **1**, 83–93 (2007).

5. Mori, M., Tiang, G. & Higuchi, K. AA amyloidosis-resistant CE/J mice have Saa1 and Saa2 genes that encode an identical SAA isoform. *Amyloid Int. J. Exp. Clin. Investig. Off. J. Int. Soc. Amyloidosis* **21**, 1–8 (2014).

6. Collinge, J. Variant Creutzfeldt-Jakob disease. *The Lancet* **354**, 317–323 (1999).

7. Hsiao, K. *et al.* Mutant prion proteins in Gerstmann-Sträussler-Scheinker disease with neurofibrillary tangles. *Nat. Genet.* **1**, 68–71 (1992).

8. Liberta, F. *et al.* Morphological and primary structural consistency of fibrils from different AA patients (common variant). *Amyloid* **26**, 164–170 (2019).

9. Tailleux, A., Duriez, P., Fruchart, J.-C. & Clavey, V. Apolipoprotein A-II, HDL metabolism and atherosclerosis. *Atherosclerosis* **164**, 1–13 (2002).

10. Prokaeva, T. *et al.* Hereditary Renal Amyloidosis Associated With a Novel Apolipoprotein A-II Variant. *Kidney Int. Rep.* **2**, 1223–1232 (2017).

11. Gursky, O. Hot spots in apolipoprotein A-II misfolding and amyloidosis in mice and men. *FEBS Lett.* **588**, 845–850 (2014).

12. Sawashita, J. *et al.* C-terminal sequence of amyloid-resistant type F apolipoprotein A-II inhibits amyloid fibril formation of apolipoprotein A-II in mice. *Proc. Natl. Acad. Sci. U. S. A.* **112**, E836-845 (2015).

13. Dai, J. *et al.* Curcumin promotes AApoAII amyloidosis and peroxisome proliferation in mice by activating the PPARα signaling pathway. *eLife* **10**, e63538 (2021).

14. Kitagawa, K. *et al.* Polymorphisms of mouse apolipoprotein A-11: seven alleles found among 41 inbred strains of mice. *Amyloid* **10**, 207–214 (2003).

15. Liu, Y. *et al.* Distribution of Transmissible Amyloid Proteins in the Liver with Apolipoprotein A-II Amyloidosis. *Shinshu Med. J.* **64**, 183–194 (2016).

16. Bansal, A. *et al.* AA amyloid fibrils from diseased tissue are structurally different from in vitro formed SAA fibrils. *Nat. Commun.* **12**, 1013 (2021).

17. Schönfelder, J. *et al.* Protease resistance of ex vivo amyloid fibrils implies the proteolytic selection of disease-associated fibril morphologies. *Amyloid* **28**, 243–251 (2021).

18. Li, D. & Liu, C. Hierarchical chemical determination of amyloid polymorphs in neurodegenerative disease. *Nat. Chem. Biol.* **17**, 237–245 (2021).

19. Falcon, B. *et al.* Novel tau filament fold in chronic traumatic encephalopathy encloses hydrophobic molecules. *Nature* **568**, 420 (2019).

20. Radamaker, L. *et al.* Cryo-EM structure of a light chain-derived amyloid fibril from a patient with systemic AL amyloidosis. *Nat. Commun.* **10**, 1103 (2019).

21. Westermark, G. T., Fändrich, M. & Westermark, P. AA amyloidosis: pathogenesis and targeted therapy. *Annu. Rev. Pathol.* **10**, 321–344 (2015).

22. Weissmann, C. & Flechsig, E. PrP knock-out and PrP transgenic mice in prion research. *Br. Med. Bull.* **66**, 43–60 (2003).

23. Zhang, W. *et al.* Heparin-induced tau filaments are polymorphic and differ from those in Alzheimer's and Pick's diseases. *eLife* **8**, e43584 (2019).

24. Kollmer, M. *et al.* Cryo-EM structure and polymorphism of Aβ amyloid fibrils purified from Alzheimer's brain tissue. *Nat. Commun.* **10**, 4760 (2019).

25. Radamaker, L. *et al.* Role of mutations and post-translational modifications in systemic AL amyloidosis studied by cryo-EM. *Nat. Commun.* **12**, 6434 (2021).

26. Higuchi, K. *et al.* Fibrilization in mouse senile amyloidosis is fibril conformation-dependent. *Lab. Investig. J. Tech. Methods Pathol.* **78**, 1535–1542 (1998).

27. Xing, Y. *et al.* Transmission of Mouse Senile Amyloidosis. *Lab. Invest.* **81**, 493–499 (2001).

28. Miyahara, H. *et al.* Macrophages in the reticuloendothelial system inhibit early induction stages of mouse apolipoprotein A-II amyloidosis. *Amyloid Int. J. Exp. Clin. Investig. Off. J. Int. Soc. Amyloidosis* 1–14 (2022) doi:10.1080/13506129.2022.2153667.

29. MASH Explorer: A Universal Software Environment for Top-Down Proteomics - PubMed. https://pubmed.ncbi.nlm.nih.gov/32786689/.

30. Schindelin, J. *et al.* Fiji: an open-source platform for biological-image analysis. *Nat. Methods* **9**, 676–682 (2012).

31. Zheng, S. Q. *et al.* MotionCor2: anisotropic correction of beam-induced motion for improved cryo-electron microscopy. *Nat. Methods* **14**, 331–332 (2017).

32. Rohou, A. & Grigorieff, N. CTFFIND4: Fast and accurate defocus estimation from electron micrographs. *J. Struct. Biol.* **192**, 216–221 (2015).

33. Scheres, S. H. W. Amyloid structure determination in RELION-3.1. *Acta Crystallogr. Sect. Struct. Biol.* **76**, 94–101 (2020).

34. Emsley, P., Lohkamp, B., Scott, W. G. & Cowtan, K. Features and development of Coot. *Acta Crystallogr. D Biol. Crystallogr.* **66**, 486–501 (2010).

35. Adams, P. D. *et al.* PHENIX: a comprehensive Python-based system for macromolecular structure solution. *Acta Crystallogr. D Biol. Crystallogr.* **66**, (2010).

36. Williams, C. J. *et al.* MolProbity: More and better reference data for improved all-atom structure validation. *Protein Sci. Publ. Protein Soc.* **27**, 293–315 (2018).

37. Wriggers, W. Conventions and workflows for using Situs. *Acta Crystallogr. D Biol. Crystallogr.* **68**, 344–351 (2012).

38. Pettersen, E. F. *et al.* UCSF Chimera--a visualization system for exploratory research and analysis. *J. Comput. Chem.* **25**, (2004).

39. Lee, J. *et al.* CHARMM-GUI Membrane Builder for Complex Biological Membrane Simulations with Glycolipids and Lipoglycans. *J. Chem. Theory Comput.* **15**, 775–786 (2019).

40. Lindorff-Larsen, K. *et al.* Improved side-chain torsion potentials for the Amber ff99SB protein force field. *Proteins* **78**, 1950–1958 (2010).

41. Horn, H. W. *et al.* Development of an improved four-site water model for biomolecular simulations: TIP4P-Ew. *J. Chem. Phys.* **120**, 9665–9678 (2004).

42. Mamatkulov, S. & Schwierz, N. Force fields for monovalent and divalent metal cations in TIP3P water based on thermodynamic and kinetic properties. *J. Chem. Phys.* **148**, 074504 (2018).

43. Schwierz, N., Frost, C. V., Geissler, P. L. & Zacharias, M. Dynamics of Seeded Aβ40-Fibril Growth from Atomistic Molecular Dynamics Simulations: Kinetic Trapping and Reduced Water Mobility in the Locking Step. *J. Am. Chem. Soc.* **138**, 527–539 (2016).

44. Van Der Spoel, D. *et al.* GROMACS: fast, flexible, and free. *J. Comput. Chem.* **26**, 1701–1718 (2005).

Figures and Figure Legends

Figure 1

Figure 1. Length variation of the AApoAII fibril proteins.

Amino acid sequence of the fibril precursor protein ApoA-II shown side-by-side with the protein fibril fragments (grey bars) in each sample. Red: pyroglutamate (Z). Yellow: methionine. Black residues indicate an ambiguous assignment (see Supplementary Tables 1-4). The letters (a to f) at the left of the bars refer to the mass spectrometric peak groups a to f as indicated in Supplementary Fig. 2.

Figure 2

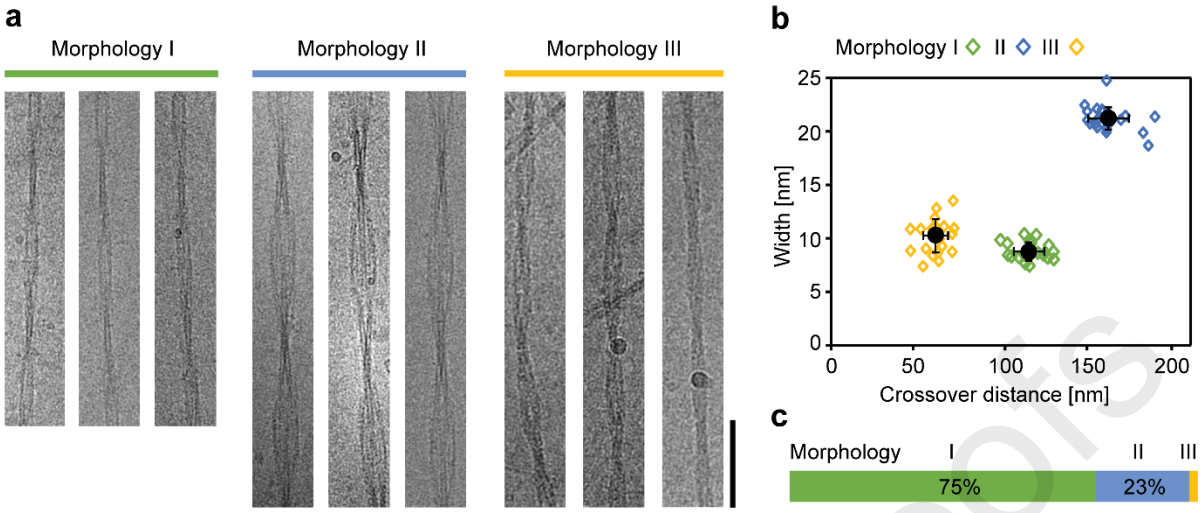

Figure 2. Morphological composition of AApoAII amyloid fibrils.

(a) Cryo-EM images of fibril Morphologies I-III, isolated from mouse tissue. Scale bar: 100 nm. The images are representative for the fibrils on 3,084 micrographs and from four animals. (b) Width and crossover distances of fibril Morphologies I to III, measured from cryo-EM images. Black: mean values (n = 20); error bars: standard deviation, open diamonds: values of the individual fibrils. Morphologies I to III are represented in different colours as indicated in the panel. (c) Morphological composition of the sample as determined from cryo-EM images of 500 fibrils. The colour code is the same as in panel (b).

Figure 3

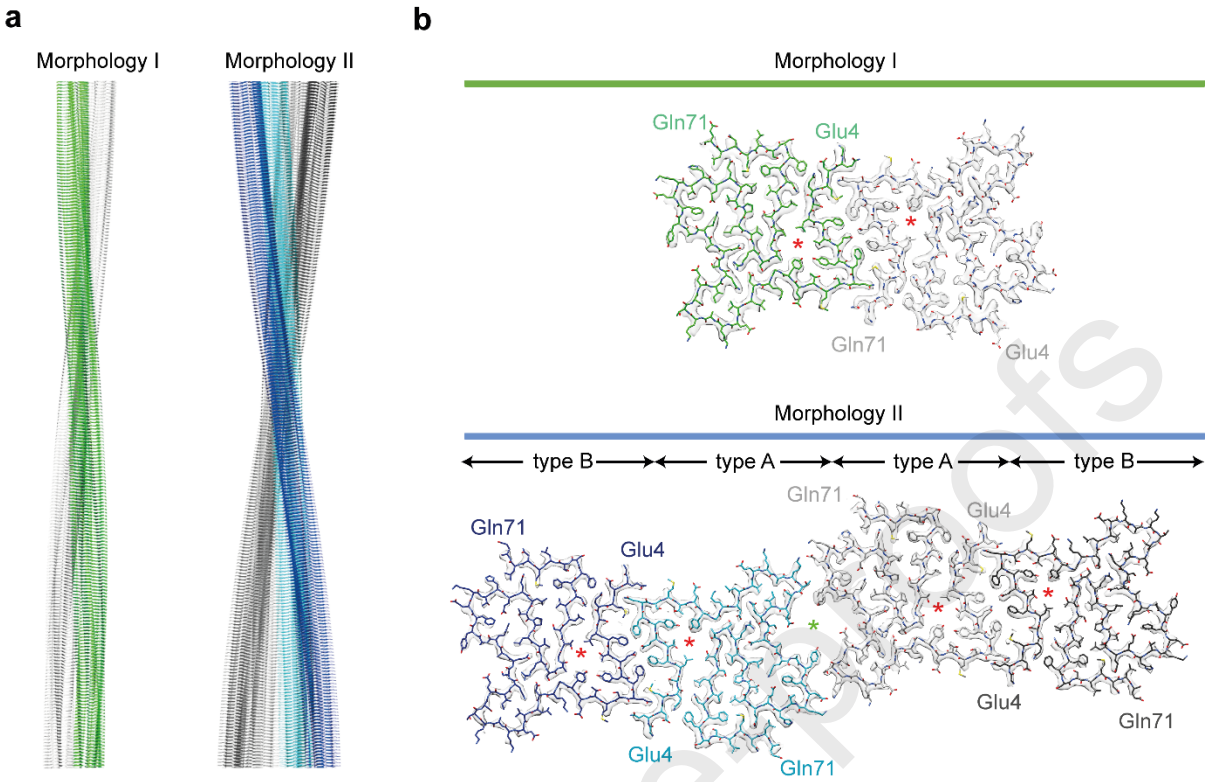

Figure 3. 3D maps and molecular models of fibril Morphologies I and II.

(a) Side views of the molecular models of Morphologies I and II. (b) Cross-sectional views of one molecular layer of the two fibrils. The 3D maps (surface rendered) are superimposed with the molecular models (stick representation). While Morphology I contains two identical protein stacks, Morphology II contains four protein stacks that can be subdivided into two types (A and B). There are two types of internal cavities marked with red and green asterisks.

Figure 4

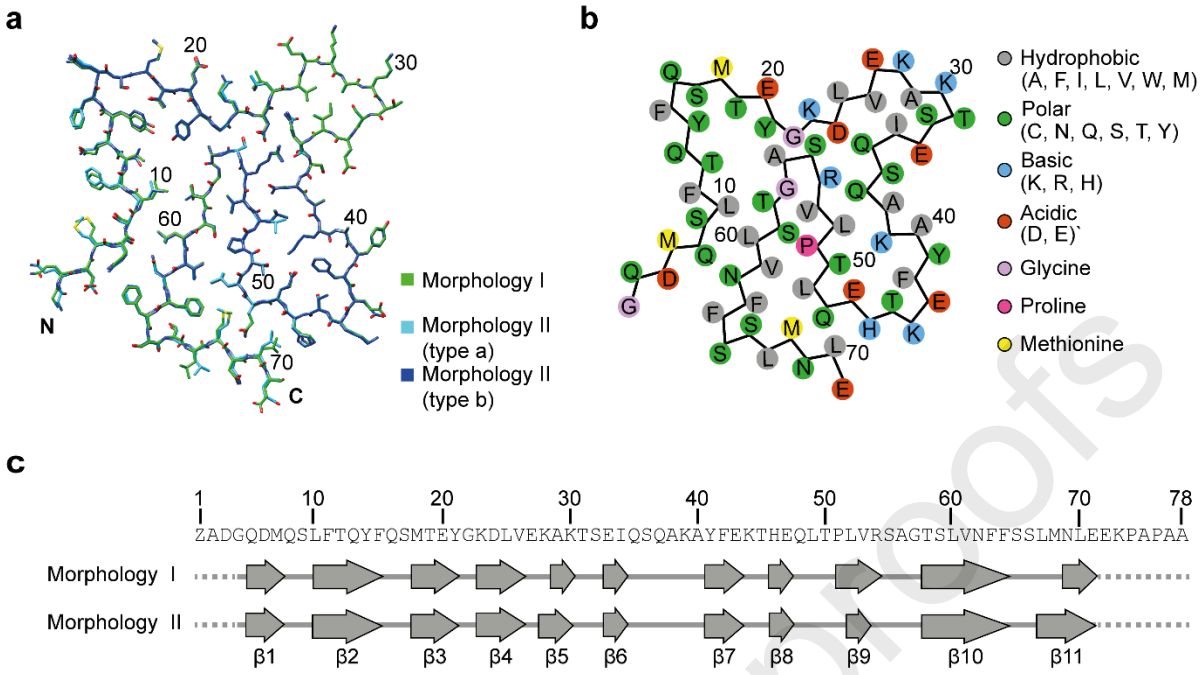

Figure 4. Fibril protein fold in Morphologies I and II.

(a) Superimposition of the fibril proteins of Morphologies I and II (types A and B) as indicated in the figure. (b) Schematic representation of the protein fold. (c) Amino acid sequence and β-strands (arrows) β1 to β11 of the fibril proteins of Morphologies I and II. The two fibril protein stacks of Morphology II share the same β-strand structure. Continuous line: residues of the fibril core. Dotted lines: disordered segments of the fibril protein not seen by cryo-EM. Z refers to pyroglutamate.

Figure 5

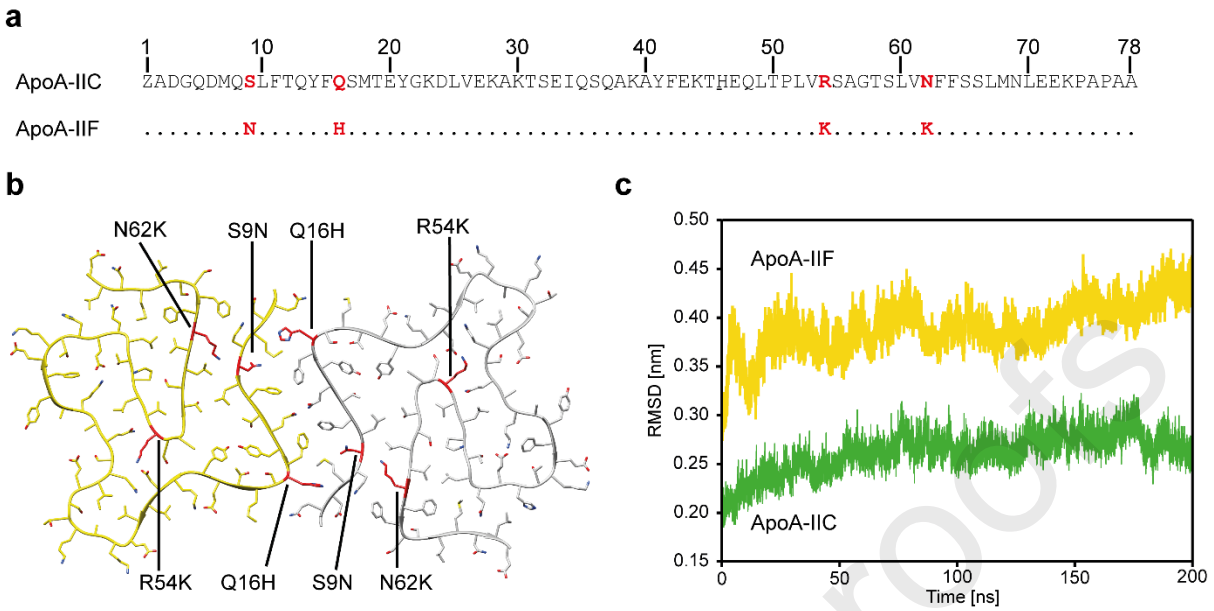

Figure 5. Comparison between the AApoAIIC reconstructed amyloid fibril and the homology model based on ApoA-IIF sequence.

(a) Amino acid sequences of ApoA-IIC and ApoA-IIF. (b) Cross-section of a homology model of a hypothetical fibril based on ApoA-IIF. The mutations compared to the experimentally determined structure are highlighted in red. (c) RMSD trajectory from the MD simulation of the reconstructed ex vivo fibril (green), and the ApoA-IIF based homology model (yellow).

Graphical Abstract

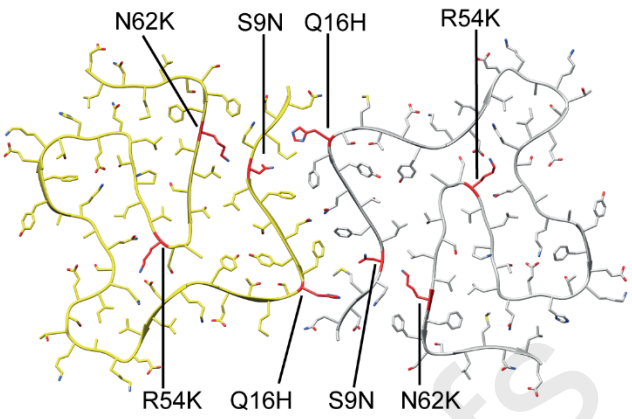

Highlights

- Mice expressing ApoA-IIF rather than ApoA-IIC are resistant to AApoAII amyloidosis
- Cryo-EM structures of ApoA-IIC-derived fibrils reveal the pathogenic fibril fold
- The mutations in ApoA-IIF destabilise the fold of the fibril proteins.
- Our data explain previous observation of the importance of the Asn62Lys mutation.
- Our study supports the idea that disease arises from specific fibril morphologies.

Declarations of interest

The authors declare that they have no conflict of interest.